2024 IEEE 63rd Conference on Decision and Control (CDC)
December 16-19, 2024. MiCo, Milan, Italy

Optimizing Parameter Design with Frequency and Clock Drift Constraints in Microgrids*

Chang Yu[1] and Xiaoqing Lu[2,*]

***Abstract*— Microgrids subjected to secondary cooperative control encounter significant challenges, including operational constraints and clock drifts, adversely affecting their stability and efficiency. This paper provides conditions that assure optimal microgrid performance in both transient and steady-state scenarios, focusing on the effects of clock drifts and fluctuations in load. Furthermore, we introduce a novel approach for designing secondary control parameters, specifically engineered to minimize steady-state discrepancies attributable to clock drifts while ensuring adherence to standards for transient operations. Comprehensive experimental validations corroborate the effectiveness of our proposed solutions.**

I. Introduction

Control performance in transient states is vital for microgrid stability at all levels. Low-inertia microgrids, for example, face significant frequency stability challenges due to rapid rate of change of frequency (RoCoF) and frequency deviations from power imbalances [4], [5]. Given microgrids' dynamic nature, fluctuations in load, generation, or transmission can push state variables beyond safe limits [1], necessitating solutions for frequency constraint [2] to maintain operation stability [3]. Innovations addressing these issues include distributed secondary control for dynamic microgrids [6], frequency-constrained energy management [7], scheduling with synthetic inertia for renewable uncertainties [8], and optimizing DG output for economic and capacity alignment [9].

The prevalence of crystal oscillator-based clocks in microgrid converters introduces clock drift risks, significantly impacting frequency control and power sharing in the secondary control layer [9]–[13]. Despite droop-controlled VSIs' resilience, they still face steady-state power distribution issues due to drifts [11]. Studies have explored the effects of clock drifts on islanded microgrids [10], highlighting potential stability risks [14] and suggesting secondary controller adjustments for enhanced stability [15]. A consensus-based algorithm has also been proposed to improve synchronization in multi-inverter microgrids facing clock drift challenges [16].

This paper addresses the challenges of dynamic operational constraints and the impact of clock drifts on stability and performance in microgrids under secondary cooperative control. It highlights the issues of secondary frequency regulation and power-sharing controls affected by clock drifts and proposes a unified modeling framework to tackle these problems. We focus on developing tuning and design strategies for secondary cooperative control that adhere to operational constraints and minimize errors due to clock drifts. The key contributions of this paper include: 1) Establishment of robust conditions for managing transient and steady-state operations amidst clock drifts and load changes, incorporating a source-load coupling mechanism to enhance system dynamics; 2) Development of a cooperative secondary control parameter tuning algorithm that reduces steady-state errors from clock drifts while maintaining compliance with transient operational constraints.

The flow of this paper is as follows: Section II introduces the modeling of microgrids considering clock drift, Section III provides the parameter conditions for meeting relevant performance metrics, and the final section presents simulation experiments for validation.

II. Preliminaries and Problem Statement

This paper adopts the following notations for vectors and matrices. $|v|$ denotes the cardinality of set v. Matrices filled with all ones and zeros are denoted as $\mathbf{1}_{n\times m}$ and $\mathbf{0}_{n\times m}$ in $\mathbb{R}^{n\times m}$, respectively. The identity matrix is $\boldsymbol{I}_n$ in $\mathbb{R}^{n\times n}$. The diagonal matrix formed from elements x_i for $i \in \mathcal{N}$ is $\mathrm{diag}\left([x_i]_{i\in\mathcal{N}}\right)$. The infinite norm of vector x and matrix A are $\|x\|_\infty$ and $\|A\|_\infty$, respectively. The vectorized sine function over x is $\sin(x)$. Vector comparison $x < y$ (or $x \le y$) means element-wise comparison. For $A \in \mathbb{R}^{m\times n}$, A^{P} and A^{N} are defined as $A^{\mathrm{P}}_{ij} = \max(A_{ij}, 0)$ and $A^{\mathrm{N}}_{ij} = \min(A_{ij}, 0)$. For $A \in \mathbb{R}^{m\times m}$, A^+has $A^+_{ij} = A_{ij}$ for $i \ne j$ and $A^+_{ij} = 0$ for $i = j$, while A^0 has $A^0_{ij} = A_{ij}$ for $i \ne j$ and $A^0_{ij} = 0$ for $i = j$.

Denote the clock period of DG$_i$'s processor as Δt_i, with the nominal period as Δt and relative drift as μ_i, where $\Delta t_i = (1+\mu_i)\Delta t$. Assuming μ_i remains constant over time, the integration step size in the cyber network, ε_i, and the time signal, $t_i = k\varepsilon_i$, are proportional to Δt. If ε is the step size in nominal clock time, then for all DG$_i$, $t_i = (1+\mu_i)t = k(1+\mu_i)\varepsilon$ with positive integer k. This leads to the derivative relation $\frac{d(\cdot)}{dt_i} = \frac{1}{1+\mu_i}\frac{d(\cdot)}{dt}$. Therefore, at nominal time t, the corrected state $x_i^*(t) = \frac{1}{1+\mu_i}x_i(t) = \gamma_i x_i(t)$, where x_i^* and

*This work was supported in part by the National Natural Science Foundation of China under Grant Nos. 62103310, 62322313, and 62173257; in part by the Open Fund of the Key Laboratory of Image Processing and Intelligent Control (Huazhong University of Science and Technology), Ministry of Education, 2022; and in part by the Fundamental Research Funds for the Central Universities under Grant 20422024kf1004

*Corresponding author

[1]C. Yu is with the School of Information Science and Engineering, Wuhan University of Science and Technology, Wuhan 430081, China, and also with the Key Laboratory of Image Processing and Intelligent Control(Huazhong University of Science and Technology), Ministry of Education, Wuhan, 430074, China yuchang@wust.edu.cn

[2]X. Lu is with the School of Electrical Engineering and Automation, Wuhan University, Wuhan, 430000, China luxq@whu.edu.cn

x_i are the states in local and nominal times, respectively, and γ_i is the clock drift coefficient. For simplicity, all derivative discussions will refer to nominal time, i.e., $d(\cdot)/dt$.

For the AC microgrid's physical network, we define a simple undirected graph $\mathcal{G}_p(\mathcal{V},\mathcal{E},\mathcal{A})$, where $\mathcal{V}=\{1,\cdots,n\}$ represents nodes with m DGs and $n-m$ loads, $\mathcal{E}\subseteq\mathcal{V}\times\mathcal{V}$ the physical links, and $\mathcal{A}\in\mathbb{R}^{n\times n}$ the adjacency matrix, with $a_{ij}>0$ for edges $e=(i,j)\in\mathcal{E}$ and $a_{ij}=0$ otherwise. The incidence matrix B_p and weighted Laplacian matrix L_p are derived, with $\mathcal{N}_i=\{j\in\mathcal{V}:(i,j)\in\mathcal{E}\}$ indicating DG_i 's physical neighbors. DGs and loads are denoted by $\mathcal{V}_G$ and $\mathcal{V}_L$, respectively. In the cyber network, DGs communicate via a directed graph $\mathcal{G}_c(\widetilde{\mathcal{V}},\tilde{\mathcal{E}},\tilde{\mathcal{A}})$, sharing the same DG node set $\widetilde{\mathcal{V}}=\mathcal{V}$, with cyber links $\tilde{\mathcal{E}}$, adjacency matrix $\widetilde{\mathcal{A}}$, and leader adjacency matrix $\Lambda=\mathrm{diag}([\widetilde{a}_{i0}]_{i\in\mathcal{V}})$. A DG accesses the virtual leader DG_0 's state if $\widetilde{a}_{i0}>0$. The cyber neighbor set is $\widetilde{\mathcal{N}}_i$, and the Laplacian matrix L_c reflects the directed nature of $\mathcal{G}_c$. The network satisfies the detailed balance condition with positive vectors $\tilde{\xi}$, ensuring $\tilde{\xi}_k\tilde{a}_{k\ell}=\tilde{\xi}_\ell\tilde{a}_{\ell k}$ for all $k,\ell\in\widetilde{\mathcal{V}}$.

A. Dynamic of Isolated Cyber-physical Microgrids

We've implemented frequency-droop controllers in an isolated AC microgrid, enabling DGs to supply power to loads and contribute to the grid. This approach modifies traditional frequency-droop control to account for clock drifts,

$$\omega_i^*(t)=\gamma_i\omega_i(t)=\omega_{\mathrm{nom}}^i(t)-K_i^P P_i(t)-K_i^D dP_i/dt_i, \tag{1}$$

for $i\in\mathcal{V}_G$, where ω_{nom}^i is the active power nominal set-point of the internal inverter frequency, ω_i^* and ω_i are DG_i's frequencies concerning the local time and nominal time, K_i^P is the droop coefficient. The final term, $-K_i^D\frac{dP_i}{dt_i}$, represents a negative feedback mechanism originating from the variations in the inverter power angle. P_i represents the measured active power that is injected into the microgrid at bus i, and is obtained by

$$P_i(t)=G_{\mathrm{LPF},i}(s)P_{E,i}(t), \tag{2}$$

where $G_{\mathrm{LPF},i}(s)=\omega_c^i\left(s+\omega_c^i\right)^{-1}$ is a low-pass filter with cutoff frequency ω_{c}^i for measuring power, and $P_{E,i}$ is the instantaneous active power, calculated as $P_{E,i}=\sum_{i\in\mathcal{N}_i}E_iE_j\left|Y_{ij}\right|\sin\left(\theta_i-\theta_j\right)$, where E_i is the voltage magnitude.

Under the effect of clock drifts the relationship between P_i and $P_{E,i}$ as a differential equation can be expressed as

$$\gamma_i\dot{P}_i(t)+\omega_c^iP_i(t)=\omega_c^iP_{E,i}(t) \tag{3}$$

The dynamics of the loads can be modeled by the following Kuramoto-like equations, for $i\in\mathcal{V}_L$,

$$0=-P_{L,i}-\sum\nolimits_{i\in\mathcal{N}_i}E_iE_j\left|Y_{ij}\right|\sin\left(\theta_i-\theta_j\right), \tag{4}$$

where Y_{ij} is the admittance of the physical link between nodes i and j, for all the nodes. $P_{L,i}>0$ is the power demand of load node i, for $i\in\mathcal{V}_L$. For simplicity, we denote the dynamical coupling strength $a_{ij}=V_iV_j\left|Y_{ij}\right|\in\mathbb{R}$ for different physical link $e=(i,j)\in\mathcal{E}$. Suppose the system solution (1-3) is frequency-synchronized. In that case, there exists ω_{syn} which characterizes the steady-state frequency of the system and is expected to be equal to the rated value, $\omega^{\mathrm{ra}}=50$ or 60Hz.

Let $\omega_{\mathrm{nom}}=\left[\omega_{\mathrm{nom}}^i\right]_{i\in\mathcal{V}_G}$, $\theta=[\theta_i]_{i\in\mathcal{V}}$, $\widehat{\omega}=\dot{\theta}=[\omega_i]_{i\in\mathcal{V}}$, $\omega=[\omega_i]_{i\in\mathcal{V}_G}$, $P=[P_i]_{i\in\mathcal{V}}$, $P_E=[P_{E,i}]_{i\in\mathcal{V}_G}$, $P_L=[P_{L,i}]_{i\in\mathcal{V}_L}$, $K_P=\mathrm{diag}\left(\left[K_i^P\right]_{i\in\mathcal{V}_G}\right)$, $K_D=\mathrm{diag}\left(\left[m_i^D\right]_{i\in\mathcal{V}_G}\right)$, $\Upsilon=\mathrm{diag}\left([\gamma_i]_{i\in\mathcal{V}_G}\right)$, $\mathcal{T}=\mathrm{diag}\left(\left[1/\omega_c^i\right]_{i\in\mathcal{V}_G}\right)$ and $W=\mathrm{diag}\left(\left[K_e\right]_{e=(i,j)\in\mathcal{E}}\right)\in\mathbb{R}^{|\mathcal{E}|\times|\mathcal{E}|}$ with $K_e=E_iE_j|Y_{ij}|$.

With the implementation of secondary controllers, the nominal set points for each DG_i with $i\in\mathcal{V}_G$, can be effectively calculated as

$$\omega_{\mathrm{nom}}^i(t)=c\int_0^t\left[u_i^\omega(t)+u_i^P(t)\right]dt, \tag{5}$$

where $u_i^\omega(t)$ and $u_i^P(t)$ are respectively the frequency and active power control laws which are the inputs in front of the integrators, and $c>0$ is the coupling strength. Next, combine (2) and (3), we obtain the power flow equation in matrix form. Then, derive the equation concerning nominal time t to obtain

$$\frac{d}{dt}\begin{bmatrix}P_E^T & -P_L^T\end{bmatrix}^T=B_pW\cos\left(B_p^T\theta(t)\right)B_p^T\widehat{\omega}. \tag{6}$$

We denote $\widetilde{L}(\theta(t))=B_pW\cos\left(B_p^T\theta(t)\right)B_p^T\in\mathbb{R}^{n\times n}$ which is a dynamic matrix over time signal t, and always satisfies all the characteristics of the Laplacian matix. If we partition the matrix $\widetilde{L}(\theta(t))$ into the 2×2 form with the blocks $\widetilde{L}_{11}(t)\in\mathbb{R}^{m\times m}$, $\widetilde{L}_{12}(\theta(t))\in\mathbb{R}^{m\times(n-m)}$, $\widetilde{L}_{21}(\theta(t))\in\mathbb{R}^{(n-m)\times m}$, and $\widetilde{L}_{22}(\theta(t))\in\mathbb{R}^{(n-m)\times(n-m)}$. By solving (5), we obtain the equivalent system,

$$\dot{P}_E=\widehat{L}_{11}(\theta(t))\omega(t)-\widetilde{L}_{12}(\theta(t))\widetilde{L}_{22}^{-1}\dot{P}_L, \tag{7}$$

where $\widetilde{L}_{11}(\theta(t))-\widetilde{L}_{12}(\theta(t))\widetilde{L}_{22}^{-1}(\theta(t))\widetilde{L}_{21}(\theta(t))$, denoted as $\widehat{L}_{11}(t)$, is also a dynamical Laplacian matrix, and $\widetilde{L}_{12}(t)\widetilde{L}_{22}^{-1}(\theta(t))$ is denoted as $\mathcal{S}(t)\in\mathbb{R}^{m\times(n-m)}$ for simplicity.

By applying (1)-(7), we can obtain the microgrid dynamic system considering clock drifts,

$$\Upsilon\omega(t)=\omega_{\mathrm{nom}}(t)-K_PP(t)-\Upsilon K_D\dot{P}(t) \tag{8a}$$

$$\Upsilon\mathcal{T}\dot{P}(t)=-P(t)+P_E(t) \tag{8b}$$

$$\dot{P}_E=\widehat{L}_{11}(t)\omega(t)-\widetilde{L}_{12}(t)\widetilde{L}_{22}^{-1}\dot{P}_L \tag{8c}$$

$$\Upsilon\dot{\omega}_{\mathrm{nom}}(t)=c\left[u_i^\omega(t)+u_i^P(t)\right]. \tag{8d}$$

B. Steady-state Error and Operation Constraint

The frequency regulator aims to align each DG_i's frequency with the rated value ω^{ra}, while a power regulator ensures equitable active power distribution among DGs. Clock drift introduces steady-state deviations in both frequency and power allocation, which are sought to be minimized [10]. The tolerances for these deviations are denoted by $\kappa_1>0$ for frequency and $\kappa_2>0$ for power. Then, the controllers in (5) can be designed to regulate the active power nominal set-points in (1), such that the system terminal outputs, $\omega_i(t)$ and $P_i(t)$, achieve the following control objectives,

$$\left\{\begin{array}{l}\lim_{t\to\infty}\left|\omega_i(t)-\omega^{\mathrm{ra}}\right|\le\kappa_1,\quad \text{for } i\in\mathcal{V}_G\\ \lim_{t\to\infty}\left|K_i^P P_i(t)-K_j^P P_j(t)\right|\le\kappa_2,\quad (i,j)\in\widetilde{\mathcal{E}}\end{array}\right.\tag{9}$$

where the droop coefficients are selected as $K_i^P P_i^{\max}=K_j^P P_j^{\max}$ for $i,j\in\mathcal{V}_G$, and $P_i^{\max}$ is the maximum capacity of DG_i.

During regulation, each DG's frequency must stay within a specified range, with $\omega_i(t)$'s trajectories confined to a set in $\mathbb{R}^n$:

$$\Omega_1=\left\{\omega_i\in\mathbb{R}:-\overline{\omega}\le\omega_i-\omega^{\mathrm{ra}}\le\overline{\omega},\quad \overline{\omega}\in\mathbb{R}_+\right\}.\tag{10}$$

Without loss of generality, $\overline{\omega}\mathbf{1}_m$ is typically regarded as having identical elements.

III. Secondary Control Considering the Constraint and Clock Drift

A. Cooperative Control with Clock Drifts

The control input, u_i^ω, is designed using neighboring DGs' output differences. The main objective is to develop a distributed control protocol, denoted as $u_i^\omega(t)$, for the system (8) such that $\lim_{t\to\infty}\left|\omega_i(t)-\omega^{\mathrm{ra}}\right|=0$, then one can write,

$$\begin{aligned}u_i^\omega(t)=&k_1^i\widetilde{\vartheta}_{i0}a_{i0}\left[\omega^{\mathrm{ra}}-\omega_i^*(t)\right]\\&+k_2^i\sum\nolimits_{j\in\widetilde{\mathcal{N}}_i}\widetilde{\vartheta}_{ij}a_{ij}\left[\omega_j^*(t)-\omega_i^*(t)\right]\\=&k_1^i\widetilde{\vartheta}_{i0}a_{i0}\left[\omega^{\mathrm{ra}}-\gamma_i\omega_i(t)\right]\\&+k_2^i\sum\nolimits_{j\in\widetilde{\mathcal{N}}_i}\widetilde{\vartheta}_{ij}a_{ij}\left[\gamma_j\omega_j(t)-\gamma_i\omega_i(t)\right]\end{aligned}\tag{11}$$

with the leader adjacency matrix Λ and the corresponding gain matrix $\Xi=\mathrm{diag}\left(\widetilde{\vartheta}_{10},\cdots,\widetilde{\vartheta}_{m0}\right)\cdot\mathrm{DG}_i$ can access ω^{ra} if and only if $a_{i0}>0$. $\Theta=[\widetilde{\vartheta}_{s\ell}]_{m\times m}$ is the positive gain matrices corresponding to the cyber network's adjacency matrix $\widetilde{\mathcal{A}}=[\tilde{a}_{s\ell}]_{m\times m}$, k_1^i and k_2^i are positive control gains to be designed.

The consensus-based power controllers are as follows:

$$u_i^P(t)=k_3^i\sum\nolimits_{j\in\widetilde{\mathcal{N}}_i}\widetilde{\vartheta}_{ij}\tilde{a}_{ij}\left[K_j^P P_j(t)-K_i^P P_i(t)\right],\tag{12}$$

where k_3^i is the positive control gain. Since the considered cyber network graphs are directed, the corresponding matrix L_c may be asymmetric. However, by the detailed balance assumption, one can always choose the gain matrices Φ to ensure the symmetries of $L_c\odot\Theta$.

Combine (11) and (12), we have the following compact form,

$$\left\{\begin{array}{l}u^\omega(t)=-\left[K_1(L_c\odot\Theta)+K_2\Lambda\odot\Xi\right]\left(\Upsilon\omega(t)-\omega^{\mathrm{ra}}\mathbf{1}_m\right)\\ u^P(t)=-K_3(L_c\odot\Theta)K_P P\end{array}\right..\tag{13}$$

where $K_1=\mathrm{diag}\left(\left[k_1^i\right]_{i\in\mathcal{V}_G}\right)$, $K_2=\mathrm{diag}\left(\left[k_2^i\right]_{i\in\mathcal{V}_G}\right)$ and $K_3=\mathrm{diag}\left(\left[k_3^i\right]_{i\in\mathcal{V}_G}\right)\in\mathbb{R}^{m\times m}$ denote the control gain matrix, which is to be designed such that the system can make the constraints associated with frequencies and clock drift satisfied.

In this case, system (8) can be rewritten by plugging in u_i^ω and u_i^P in (11) and (12),

$$\begin{aligned}\Upsilon\dot{\omega}(t)=&-c\Upsilon^{-1}\left(K_1L_c\odot\Theta+K_2\Lambda\odot\Xi\right)\left(\Upsilon\omega(t)\right.\\&\left.-\omega^{\mathrm{ra}}\mathbf{1}_m\right)-c\Upsilon^{-1}K_3L_c\odot\Theta K_P P(t)-K_P\dot{P}(t)\\&-\Upsilon K_D\ddot{P}(t)\end{aligned}\tag{14a}$$

$$\Upsilon\mathcal{T}\dot{P}(t)=-P(t)+P_E(t)\tag{14b}$$

$$\dot{P}_E=\widehat{L}_{11}(t)\omega(t)-\widetilde{L}_{12}(t)\widetilde{L}_{22}^{-1}\dot{P}_L\tag{14c}$$

$$\begin{aligned}\Upsilon\dot{\omega}_{\mathrm{nom}}(t)=&-c\left[\left(K_1L_c\odot\Theta+K_2\Lambda\odot\Xi\right)\left(\Upsilon\omega(t)-\omega^{\mathrm{ra}}\mathbf{1}_m\right)\right.\\&\left.+K_3L_c\odot\Theta K_P P\right].\end{aligned}\tag{14d}$$

In the steady state, the left-hand side of all equations in (14) equals zero. By (14d), we have

$$\begin{aligned}&\left(K_1L_c\odot\Theta+K_2\Lambda\odot\Xi\right)\left(\Upsilon\omega_{\mathrm{syn}}\mathbf{1}_m-\omega^{\mathrm{ra}}\mathbf{1}_m\right)\\&\qquad+K_3L_c\odot\Theta K_P P^s=\mathbf{0}_m,\end{aligned}\tag{15}$$

where P^s is the steady-state of $P(t)$ and $P_E(t)$ which is related to the final load state P_L^s. It is easily obtained the synchronous frequency ω_{syn} as

$$\omega_{\mathrm{syn}}=\frac{\mathbf{1}_m^TK_3^{-1}K_2\Lambda\odot\Xi\mathbf{1}_m}{\mathbf{1}_m^TK_3^{-1}(K_2\Lambda\odot\Xi+K_1L_c\odot\Theta)\Upsilon\mathbf{1}_m}\omega^{\mathrm{ra}}.\tag{16}$$

The error between the synchronous frequency and the rated frequency can be expressed as

$$\Delta\omega=-\omega_{\mathrm{syn}}+\omega^{\mathrm{ra}}=s/(q+s),\tag{17}$$

where $s=\mathbf{1}_m^TK_3^{-1}(K_2\Lambda\odot\Xi+K_1L_c\odot\Theta)(\Upsilon-\boldsymbol{I}_m)\mathbf{1}_m$ and $q=\mathbf{1}_m^TK_3^{-1}K_2\Lambda\odot\Xi\mathbf{1}_m$. $q\neq 0$, and $\Delta\omega$ converge to zero if and only if the value of s approaches 0.

By left-multiplying (15) with $B_c^T(L_c\odot\Theta)^\dagger K_3^{-1}$. Here, B_c denotes the corresponding incidence matrix of $L_c\odot\Theta$. Further, we substitute the steady-state value P^s into (15), and obtain

$$\begin{aligned}&-B_c^T(L_c\odot\Theta)^\dagger K_3^{-1}\left[K_1L_c\odot\Theta+K_2\Lambda\odot\Xi\right]\times\\&\left(\Upsilon\omega_{\mathrm{syn}}\mathbf{1}_m-\omega^{\mathrm{ra}}\mathbf{1}_m\right)=B_c^T(L_c\odot\Theta)^\dagger L_c\odot\Theta K_P P^s.\end{aligned}\tag{18}$$

Since $B_c^T(L_c\odot\Theta)^\dagger=B_c^\dagger$ and $B_c^T(L_c\odot\Theta)^\dagger L_c\odot\Theta=B_c^T$. These two equations transform (18) into

$$\begin{aligned}&-B_c^\dagger K_3^{-1}\left[K_1L_c\odot\Theta+K_2\Lambda\odot\Xi\right]\left(\Upsilon\omega_{\mathrm{syn}}\mathbf{1}_m-\omega^{\mathrm{ra}}\mathbf{1}_m\right)\\&=B_c^TK_PP^s.\end{aligned}\tag{19}$$

It can be seen that P^s is the solution of the combination of linear matrix equations (15) and $\mathbf{1}_m^TP^s=P_L^s$ for a given constant P_L^s. Referencing (17) and (19), we reformulate (8) as

$$\left\{\begin{array}{l}|s/(q+s)|\le\kappa_1\\ \left|B_c^\dagger K_3^{-1}(K_1L_c\odot\Theta+K_2\Lambda\odot\Xi)(\Upsilon\omega_{\mathrm{syn}}\mathbf{1}_m-\omega^{\mathrm{ra}}\mathbf{1}_m)\right|\\ \le\kappa_2\end{array}\right.\tag{20}$$

in which, the synchronization frequency, ω_{syn}, is given by (16).

$$f(\zeta,t)=\underbrace{\begin{bmatrix}-c\Upsilon^{-2}\left(K_1L_c\odot\Theta+K_2\Lambda\odot\Xi\right)\Upsilon-\Upsilon^{-1}K_D\mathcal{T}^{-1}\widehat{L}_{11}(t) & -c\Upsilon^{-2}K_3L_c\odot\Theta K_P+K_4 & -K_4 & *\\ * & -\Upsilon^{-1}\mathcal{T}^{-1} & \Upsilon^{-1}\mathcal{T}^{-1} & *\\ -c\Upsilon^{-2}\left(K_1L_c\odot\Theta+K_2\Lambda\odot\Xi\right)\Upsilon & -c\Upsilon^{-2}K_3L_c\odot\Theta K_P & * & *\\ \widehat{L}_{11}(t) & * & * & *\end{bmatrix}}_{H(t)\in\mathbb{R}^{4m\times 4m}}\zeta\left(t\right)+\underbrace{\begin{bmatrix}\Upsilon^{-1}K_D\mathcal{T}^{-1}\widetilde{L}_{12}(t)\widetilde{L}_{22}^{-1}\\ *\\ -\widetilde{L}_{12}(t)\widetilde{L}_{22}^{-1}\\ *\end{bmatrix}}_{Z(t)\in\mathbb{R}^{4m\times(n-m)}}\dot{P}_L, \tag{21}$$

B. Condition Analysis for the Microgrid Constraint

To facilitate constraint analysis, we next apply coordinate axis translation to move the equilibrium point of the system (14) to the origin. We let $\delta\omega=\omega-\omega_{\text{syn}}$, $\delta P=P-P^s$, $\delta P_E=P-P_E^s$, with P_E^s representing the steady-state of P_E. Then we obtain the fact that the dynamic of the state-error variable $\zeta\left(t\right)=[\delta\omega\left(t\right)^T,\delta P\left(t\right)^T,\omega_{\text{nom}}^T,\delta P_E\left(t\right)^T]^T\in\mathbb{R}^{4m}$ is bounded by a closed set $\mathit{\Omega}_3=[-\rho_{\min},\rho_{\max}]$ with $\rho_{\max}=[\overline{\delta\omega}^T,\overline{\delta P}^T,\overline{\omega_{\text{nom}}}^T,\overline{\delta P_E}^T]^T$ and $\rho_{\min}=[\underline{\delta\omega}^T,\underline{\delta P}^T,\underline{\omega_{\text{nom}}}^T,\underline{\delta P_E}^T]^T$. In order to satisfy constraint $\mathit{\Omega}_1$ and constraint $\mathit{\Omega}_2$, the bounds of $\delta\omega\left(t\right)$ and $\delta P\left(t\right)$ are respectively estimated as $\delta\omega\in[-\overline{\omega}\mathbf{1}_m+\Delta\omega,\overline{\omega}\mathbf{1}_m+\Delta\omega]$, $\delta P\in[-P^s,P^{\max}-P^s]$ and $\delta P_E\in[-P^s,\overline{\eta}-P^s]$ that all contain the origin within them.

The dynamic of $\zeta(t)$, $\dot{\zeta}=f(\zeta,t)$ shown in (21) follows from (14). In (21), $K_4=K_P\Upsilon^{-2}\mathcal{T}^{-1}-K_D\Upsilon^{-2}\mathcal{T}^{-2}$, all elements of the part marked with $*$ are zero. For simplicity, we let $Q(t)=-c\Upsilon^{-2}\left(K_1L_c\odot\Theta+K_2\Lambda\odot\Xi\right)\Upsilon-\Upsilon^{-1}K_D\mathcal{T}^{-1}\widehat{L}_{11}(t)$, $N=-c\Upsilon^{-2}K_3L_c\odot\Theta K_P+K_4$.

Suppose the load change rate $\dot{P}_L$ is within the range $[-\overline{\alpha},\overline{\alpha}]$ where $\overline{\alpha}$ can be estimated through historical data, we then obtain the following result,

Theorem 1. *In a microgrid with secondary controller (13), assuming load changes nullify at equilibrium with initial states $\zeta_i(0)$ in $\mathit{\Omega}_1$ and $\overline{\eta}\leq P^{\max}$, the following holds: the trajectories of ζ_i, for $i\in\mathcal{V}_G$, are bounded by $\mathit{\Omega}_1$, if*

$$-c\Upsilon^{-2}\left(K_1L_c\odot\Theta+K_2\Lambda\odot\Xi\right)\Upsilon+b\leq\mathbf{0}_m, \tag{C1}$$

with $b=\max\{N^{\mathbb{P}}\overline{\delta P}+N^{\mathbb{N}}\underline{\delta P}+K_4^{\mathbb{P}}\overline{\delta P_E}+K_4^{\mathbb{N}}\underline{\delta P_E}+\overline{\beta},N^{\mathbb{P}}\underline{\delta P}+N^{\mathbb{N}}\overline{\delta P}+K_4^{\mathbb{N}}\overline{\delta P_E}+K_4^{\mathbb{P}}\underline{\delta P_E}+\overline{\beta}\}$.

Proof: We first prove that the condition for the above constraint to hold is the satisfaction of the following inequality,

$$\begin{aligned}\max\big\{&H(t)^+\rho_{\max}+H(t)^0\rho_{\min}+\overline{Z}\overline{\alpha},\\ &H(t)^0\rho_{\max}+H(t)^+\rho_{\min}+\overline{Z}\overline{\alpha}\big\}\leq\mathbf{0}_{2m}.\end{aligned} \tag{22}$$

where $\overline{Z}=\sup Z(t)$ for $t\geq 0$. It follows from the first part of the above condition

$$H(t)^+\rho_{\max}+H(t)^0\rho_{\min}+\overline{Z}\overline{\alpha}\leq 0, \tag{23}$$

and the following inequality holds,

$$(\boldsymbol{I}_{4m}+\tau H(t)^+)\rho_{\max}+\tau H(t)^0\rho_{\min}+\tau\overline{Z}\overline{\alpha}\leq\rho_{\max}, \tag{24}$$

where τ is a positive scalar. Setting t as zero and utilizing the previous derivation, we then have

$$(\boldsymbol{I}_{4m}+\tau H(0))\zeta(0)+\tau Z\dot{P}_L(0)\leq\rho_{\max}, \tag{25}$$

yielding the following inequality,

$$(\boldsymbol{I}_{4m}+\tau H(0)^+)\rho_{\max}+\tau H(0)^0\rho_{\min}+\tau\overline{Z}\overline{\alpha}<\rho_{\max}. \tag{26}$$

Using the Taylor expansion for (21), it yields,

$$\zeta(t+\tau)=(\boldsymbol{I}_{4m}+\tau H(t))\zeta(t)+\tau Z(t)\dot{P}_L(t)+R(\tau), \tag{27}$$

where $R(\tau)$ is the remainder term. From (25) and (27), we obtain

$$\begin{aligned}\zeta(\tau)\tau&=((\boldsymbol{I}_{4m}+\tau H(0))\zeta(0)+\tau Z\dot{P}_L(0)+R(\tau))/\tau\\ &\leq(\rho_{\max}+R(\tau))/\tau.\end{aligned} \tag{28}$$

Next, we consider the inequality part of (28),

$$\zeta(\tau)/\tau<(\rho_{\max}+R(\tau))/\tau. \tag{29}$$

which can be written in a form of

$$\zeta(\tau)/\tau\leq\rho_{\max}/\tau-\kappa+R(\tau)/\tau, \tag{30}$$

where κ is a positive scalar. Since $\lim_{\tau\to 0^+}\frac{R(\tau)}{\tau}=0$, there always exists $0<\tau<\tau_1$ such that $\zeta(\tau)<\rho_{\max}$. Thus, (26) leads to $\zeta(\tau)<\rho_{\max}$. Similarly, using the other half part of the condition (22), one has,

$$\begin{aligned}&(\boldsymbol{I}_{4m}+\tau H(0))\zeta(0)+\tau Z\dot{P}_L\left(0\right)\\ &\geq-(\boldsymbol{I}_{4m}+\tau H(0)^+)\rho_{\min}-\tau H(0)^0\rho_{\max}-\tau\overline{Z}\overline{\alpha}\\ &\geq-\rho_{\min},\end{aligned} \tag{31}$$

which can be rewritten in an inequality part as

$$(\boldsymbol{I}_{4m}+\tau H(0)^+)\rho_{\min}+\tau H(0)^0\rho_{\max}+\tau\overline{Z}\overline{\alpha}<\rho_{\min}. \tag{32}$$

Mirroring the approach of (27)-(30), we deduce from (32) that $\zeta(\tau)>\rho_{\min}$. Thus, (26) and (32) guarantee the state variable stays within the open interval $(-\rho_{\min},\rho_{\max})$. We then consider a sequence of dynamics $\{f_n\}$,

$$f_n(\zeta)=\left(1-\frac{1}{n+1}\right)H(t)\zeta\left(t\right)+Z(t)\dot{P}_L,\ n=1,2,\ldots \tag{33}$$

Obviously, $\lim_{n\to\infty}f_n=f$. Denote $\left(1-\frac{1}{n+1}\right)H(t)=H_n(t)$, and $\widetilde{\zeta}^n(t)$ as the solution of the equation $\boldsymbol{I}_{4m}\dot{\zeta}(t)=f_n(\zeta)$ with the initial condition $\zeta(0)\in\mathit{\Omega}_1$. It can be inferred that, for $n=1,2,\ldots$,

$$\begin{cases}(\boldsymbol{I}_{4m}+\tau H_n(0)^+)\rho_{\max}+\tau H_n(0)^0\rho_{\min}+\tau\overline{Z}\overline{\alpha}<\rho_{\max}\\ (\boldsymbol{I}_{4m}+\tau H_n(0)^+)\rho_{\min}+\tau H_n(0)^0\rho_{\max}+\tau\overline{Z}\overline{\alpha}<\rho_{\min}\end{cases} \tag{34}$$

. By applying the same steps as above, we can arrive at that $\widetilde{\zeta}^n(t)\in\mathit{\Omega}_1$. By [17], there exists an integer n_0 such that each $\widetilde{\zeta}^n(t)$, $n\geq n_0$, converges to $\zeta(t)$ for $t\in[0,t_1]$. Then one can conclude that $\zeta(t)\in\mathit{\Omega}_1$, $t\in[0,t_1]$. In summary, condition (22) ensures the validity of conclusion $\zeta(t)\in\mathit{\Omega}_1$ for $t\geq 0$.

Substitute the upper and lower bounds $\rho_{\max}$ and $\rho_{\min}$ into the condition (22) yielding,

$$\begin{cases} Q(t)\overline{\omega}\mathbf{1}_m + N^{\mathbb{P}}\overline{\delta P} + N^{\mathbb{N}}\underline{\delta P} + K_4^{\mathbb{P}}\overline{\delta P_E} + K_4^{\mathbb{N}}\underline{\delta P_E} + \overline{\beta} \leq \mathbf{0}_m \\ Q(t)\overline{\omega}\mathbf{1}_m + N^{\mathbb{P}}\underline{\delta P} + N^{\mathbb{N}}\overline{\delta P} + K_4^{\mathbb{N}}\overline{\delta P_E} + K_4^{\mathbb{P}}\underline{\delta P_E} + \overline{\beta} \leq \mathbf{0}_m \end{cases} \tag{35}$$

where $\overline{\beta}$ is the first m rows of $\overline{Z}\overline{\alpha}$. Since $\widehat{L}_{11}(t)\overline{\omega}\mathbf{1}_m = \mathbf{0}_m$, (33) can be simplified as follows:

$$-c\Upsilon^{-2}\left(K_1 L_c \odot \Theta + K_2 \Lambda \odot \Xi\right)\Upsilon + b \leq \mathbf{0}_m, \tag{36}$$

which completes the proof. □

By the fact that $N^{\mathbb{N}} \leq cK_3(-\Upsilon^{-2}L_c \odot \Theta K_P)^{\mathbb{N}} + K_4^{\mathbb{N}}$ and $N^{\mathbb{P}} \leq cK_3(-\Upsilon^{-2}L_c \odot \Theta K_P)^{\mathbb{P}} + K_4^{\mathbb{P}}$, we can obtain the following inequality from (36),

$$-c\Upsilon^{-2}\left(K_1 L_c \odot \Theta + K_2 \Lambda \odot \Xi\right)\Upsilon + cK_3\alpha_1 + \alpha_2 \leq \mathbf{0}_m, \tag{37}$$

where $\alpha_1 = \max\{(-\Upsilon^{-2}L_c \odot \Theta K_P)^{\mathbb{N}}\underline{\delta P} + (-\Upsilon^{-2}L_c \odot \Theta K_P)^{\mathbb{P}}\overline{\delta P}, (-\Upsilon^{-2}L_c \odot \Theta K_P)^{\mathbb{P}}\overline{\delta P}\} + (-\Upsilon^{-2}L_c \odot \Theta K_P)^{\mathbb{N}}\overline{\delta P}$ and $\alpha_2 = \max\{K_4^{\mathbb{N}}(\overline{\delta P_E} + \overline{\delta P}) + K_4^{\mathbb{P}}(\underline{\delta P_E} + \underline{\delta P}) + \overline{\beta}, K_4^{\mathbb{P}}(\overline{\delta P_E} + \overline{\delta P}) + K_4^{\mathbb{N}}(\underline{\delta P_E} + \underline{\delta P}) + \overline{\beta}\}$.

Integrating constraint (9) and condition in Theorem 1 allows us to identify the necessary conditions for secondary controller design. Referencing studies on ideal clocks, incorporating real-world clock drifts significantly complicates achieving precise frequency synchronization and power allocation due to the uncertainty in drift coefficients γ_i. We model the clock drift coefficient γ_i as a random variable X with a normal distribution $N(\mu, \sigma^2)$, where μ is the mean and σ is the standard deviation. For m DGs, the mean clock drift $\bar{X}$ adheres to $N(\mu, \frac{\sigma}{\sqrt{m}})$ as per the Central Limit Theorem, indicating a reduced standard deviation with increased DG count. We denote the range of clock drift coefficients in the microgrid as $\overline{\Delta}\gamma > 0$.

Based on Theorem 1 and (9), we can obtain

$$\begin{cases} s = \phi_1\kappa_1(s+q) \\ B_c^{\dagger}K_3^{-1}(K_1 L_c \odot \Theta + K_2\Lambda \odot \Xi)\left(\Upsilon\omega_{\text{syn}}\mathbf{1}_m - \omega^{\text{ra}}\mathbf{1}_m\right) \\ \qquad\qquad = \kappa_2\phi_2\mathbf{1}_{|\widetilde{\mathcal{E}}|} \\ c\Upsilon^{-2}K_3^{-1}\left(K_1 L_c \odot \Theta + K_2\Lambda \odot \Xi\right)\Upsilon\overline{\omega}\mathbf{1}_m \\ \qquad\qquad = \phi_3(K_3^{-1}\alpha_2 + c\alpha_1) \end{cases} \tag{38}$$

where $\phi_1 \in [-1, 1]$, ϕ_2 is a diagonal matrix belonging to $\mathbb{R}^{|\widetilde{\mathcal{E}}| \times |\widetilde{\mathcal{E}}|}$ with all diagonal elements in the interval $[-1, 1]$ and ϕ_3 is a diagonal matrix belonging to $\mathbb{R}^{m\times m}$ with all diagonal elements in the interval $[1, \infty]$. Then, we have the following result,

Theorem 2. *In a microgrid with the secondary controller (13), given a large number of DGs and assuming $\mu = 1$, the conditions in Theorem 1 and (9) are satisfied if*

$$K_3^{-1}K_1 = l_1\boldsymbol{I}_m, , K_3^{-1}K_2\Lambda \odot \Xi = l_2\boldsymbol{I}_m, l_1, l_2 > 0 \tag{39a}$$

$$(\omega^{\text{ra}} + \kappa_1)||l_1\boldsymbol{I}|\widetilde{\mathcal{E}}| + l_2 B_c^{\dagger}B_c^{\dagger T}||_\infty\overline{\Delta}\gamma \leq \kappa_2 \tag{39b}$$

$$K_3^{-1}\alpha_2 + c\alpha_1 \leq \frac{c\overline{\omega}}{\gamma\max^2(\omega^{\text{ra}} + \kappa_1)}B_c\kappa_2\phi_2\mathbf{1}_{|\widetilde{\mathcal{E}}|} + \frac{l_2 c\overline{\omega}}{\gamma_{\max}^2}\gamma_{\min}\mathbf{1}_m \tag{39c}$$

Proof: Initially, consider the relationships $K_3^{-1}K_1 = l_1\boldsymbol{I}_m$ and $K_3^{-1}K_2\Lambda \odot \Xi = l_2\boldsymbol{I}_m$, where both $l_1, l_2 > 0$. It follows that $\mathbf{1}_m^T K_3^{-1}(K_2\Lambda \odot \Xi + K_1 Lc \odot \Theta)(\Upsilon - \boldsymbol{I}_m)\mathbf{1}m = l_2\sum_{i=1}^m(\gamma_i - 1)$, and $\mathbf{1}_m^T K_3^{-1}(K_2\Lambda \odot \Xi + K_1 Lc \odot \Theta)(\Upsilon - \boldsymbol{I}_m)\mathbf{1}_m + \mathbf{1}_m^T K_3^{-1}K_2\Lambda \odot \Xi\mathbf{1}_m = l_2\sum_{i=1}^m\gamma_i$. Subsequently, from (19), we deduce

$$|\omega_{\text{syn}} - \omega^{\text{ra}}| = \frac{l_2|\sum_{i=1}^m(\gamma_i - 1)|}{l_2\sum_{i=1}^m\gamma_i} = \frac{|\sum_{i=1}^m(\gamma_i - 1)|}{\sum_{i=1}^m\gamma_i}. \tag{40}$$

By the above assumption, the steady-state frequency deviation of DGs will be 0.

$$\begin{aligned} &B_c^T K_P P^s \\ &= l_1 B_c^T\left(\Upsilon\omega_{\text{syn}}\mathbf{1}_m - \omega^{\text{ra}}\mathbf{1}_m\right) + l_2 B_c^{\dagger}\left(\Upsilon\omega_{\text{syn}}\mathbf{1}_m - \omega^{\text{ra}}\mathbf{1}_m\right) \\ &= \omega_{\text{syn}}\left(l_1\boldsymbol{I}_{|\widetilde{\mathcal{E}}|} + l_2 B_c^{\dagger}B_c^{\dagger T}\right)B_c^T\Upsilon\mathbf{1}_m = \kappa_2\phi_2\mathbf{1}_{|\widetilde{\mathcal{E}}|}. \end{aligned} \tag{41}$$

Based on (39b), we can derive the inequality that provides the basis for the selection of l_1 and l_2,

$$\begin{aligned} &||B_c^T K_P P^s||_\infty = ||\omega_{\text{syn}}\left(l_1\boldsymbol{I}_{|\widetilde{\mathcal{E}}|} + l_2 B_c^{\dagger}B_c^{\dagger T}\right)B_c^T\Upsilon\mathbf{1}_m||_\infty \\ &\leq (\omega^{\text{ra}} + \kappa_1)||l_1\boldsymbol{I}_{|\widetilde{\mathcal{E}}|} + l_2 B_c^{\dagger}B_c^{\dagger T}||_\infty\overline{\Delta}\gamma \leq \kappa_2. \end{aligned} \tag{42}$$

Next, by left multiplying B_c^T to both sides of the second equality in (38), we can derive,

$$\begin{aligned} &B_c B_c^{\dagger}K_3^{-1}\left(K_1 L_c \odot \Theta + K_2\Lambda \odot \Xi\right)\left(\Upsilon\omega_{\text{syn}}\mathbf{1}_m - \omega^{\text{ra}}\mathbf{1}_m\right) \\ &= B_c B_c^{\dagger}K_3^{-1}\left(K_1 L_c \odot \Theta + K_2\Lambda \odot \Xi\right)\Upsilon\omega_{\text{syn}}\mathbf{1}_m \\ &= B_c\kappa_2\phi_2\mathbf{1}_{|\widetilde{\mathcal{E}}|}. \end{aligned} \tag{43}$$

Further, it can be obtained that,

$$\begin{aligned} &K_3^{-1}\left(K_1 L_c \odot \Theta + K_2\Lambda \odot \Xi\right)\Upsilon\overline{\omega}\mathbf{1}_m \\ &= \frac{\overline{\omega}}{\omega_{\text{syn}}}B_c\kappa_2\phi_2\mathbf{1}_{|\widetilde{\mathcal{E}}|} \\ &+ \frac{\overline{\omega}}{m}\mathbf{1}_{m\times m}K_3^{-1}\left(K_1 L_c \odot \Theta + K_2\Lambda \odot \Xi\right)\Upsilon\mathbf{1}_m. \end{aligned} \tag{44}$$

Next, we insert the aforementioned formula into the third equation in (38), and based on condition (39c), we thus obtain

$$\begin{aligned} &c\Upsilon^{-2}K_3^{-1}\left(K_1 L_c \odot \Theta + K_2\Lambda \odot \Xi\right)\Upsilon\overline{\omega}\mathbf{1}_m \\ &= \frac{c\overline{\omega}}{\omega_{\text{syn}}}\Upsilon^{-2}B_c\kappa_2\phi_2\mathbf{1}_{|\widetilde{\mathcal{E}}|} + \frac{l_2 c\overline{\omega}}{m}\Upsilon^{-2}\mathbf{1}_{m\times m}\Upsilon\mathbf{1}_m \\ &\geq K_3^{-1}\alpha_2 + c\alpha_1. \end{aligned} \tag{45}$$

The proof is completed. □

Remark 1. *Theorem 2 specifies the conditions for the parameter matrices K_1, K_2, and K_3. When these conditions are satisfied, the microgrid's steady-state error and transient constraints can be managed within acceptable limits. In designing these parameters, it is prudent to account for the worst-case scenarios. For instance, the communication topology parameters of the microgrid should be selected to ensure that condition (39) is satisfied under the most stringent conditions, the extreme variations in load change rates, or severe clock drift. As a result, the computed K_1, K_2, and K_3 will be robust enough to handle a wide range*

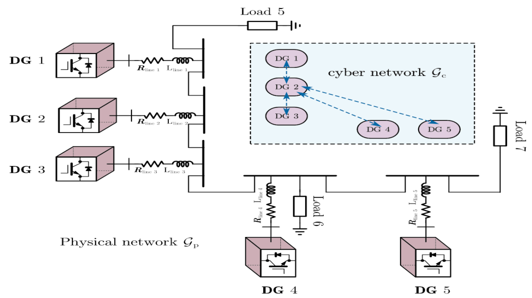

Fig. 1. Test Microgrid Schematic Diagram

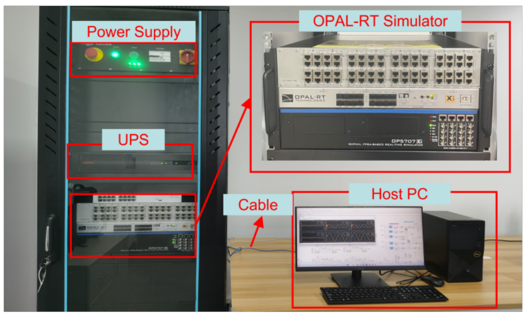

Fig. 2. Real-time experiment with OPAL-RT simulator: real-time experimental setup including the OPAL-RT target, the host PC, and Ethernet cable for networking.

of perturbations while continuously meeting the required conditions.

IV. Performance Validation

In our research, we developed a test microgrid with five DGs and three loads. Fig. 1 shows the microgrid's layout and highlights the secondary cyber network integral to its power and control systems. The DGs are interconnected via resistive-inductive lines, simulated as series RL branches. Specifications for the DGs, lines, and loads are summarized in Table I for quick reference.

As shown in Fig.2, Our tuning method's validity is demonstrated via real-time simulations on the OPAL-RT OP5707 system, connecting to a PC through LAN and interfaced by RT-LAB software with MATLAB. Our simulation unfolds in three phases. Initially, we craft a controller tailored to specific parameters. Next, we tweak its control settings to breach condition (39c), analyzing the resultant frequency and power feedback. The final phase involves adjusting parameters against condition (39b), again observing feedback for frequency and power.

TABLE I

Microgrid Inverter Simulation Parameters

Parameter	$\mathrm{DG}_{1\&3\&4}$	$\mathrm{DG}_{2\&5}$
DC Voltage V_{DC}	360 V	300 V
Maximum Current $i_i^{\max}$	$2A$	$4A$
Duty Cycle d_i	6	3
Voltage Proportional Gain $K_i^{v,PI}$	5/560	4/800
Current Proportional Gain $K_i^{i,PI}$	1.2/97	1/97
$p-f$ Droop Coefficient K_i^P	2×10^{-5}	2.8×10^{-5}
Maximum Capacity $P_i^{\max}$	14000W	14000W
Parameter	$\mathrm{Load}_{5\&6}$	Load_{7}
Active Power P	1kW	2 kW
Reactive Power Q	1kvar	1.5kvar
Parameter	$\mathrm{Line}_{1\&2\&3\&4\&5}$	
Line Resistance R_{line}	0.64Ω	
Line Inductance L_{line}	$1.32\mu H$	

This simulation methodically examines controller responses to dynamic load changes. The system load escalates from startup to a stable 48000W within 0-5 seconds, followed by oscillatory load fluctuations over the next 10 seconds. subsequently experiencing a surge and asymptotically stabilizing at a value of 66000W. Importantly, during this entire process, the rate of load variation remains confined below 26700W/s. Assuming there is clock drift in the microgrid, the clock drift coefficient is denoted as γ_i. Its mean value is 1, and the mean of $\overline{\Delta\gamma}$ is 3×10^{-5}.

Step 1: We initiated the controller tuning by setting gains l_1 and l_2, ensuring they satisfy condition (39b). With specific parameters ($\omega^{\mathrm{ra}}=50\times2\pi,\mathrm{rad/s}$, $\kappa_1=0$, $l_1=0.5$, $l_2=0.67$, $\bar{\Delta}\gamma=3.0\times10^{-5}$, and $\varpi=0.05\times2\pi,\mathrm{rad/s}$), we computed $\kappa_2=3.3\times10^{-3}\boldsymbol{I}_m$. Starting with $K_3=30\times\boldsymbol{I}_m$, we adjusted it iteratively to meet condition (39c), finalizing $K_1=15\boldsymbol{I}_m$, $K_2=20\boldsymbol{I}_m$, and $K_3=30\boldsymbol{I}_m$. Simulation results in Fig. 3 show that our tuning method stabilizes the microgrid's frequency at 50Hz, maintaining all frequencies and power allocations within prescribed limits.

Step 2: Keeping l_1 and l_2 constant, we invalidated condition (39c) by adjusting K_3 to $3\boldsymbol{I}_m$. Despite this, simulations (Fig. 4) indicate acceptable frequency synchronization and power allocation, except for transient phase frequency breaches beyond predefined limits, falling below 49.95Hz.

Step 3: For the final test, we altered $l_1=2.5$ and $l_2=5.9$ to breach condition (39b) while setting K_3 to $40\boldsymbol{I}_m$ to maintain condition (39c). The outcomes in Fig. 5 confirm stable frequency at 50Hz and adherence to frequency constraints during transient phases. However, the steady-state power allocation error surpassed the threshold, indicating a balance between meeting and missing specific conditions impacts system performance. Future work could focus on advanced clock synchronization techniques to improve microgrid stability and reliability.

V. Conclusion

In this research, we tackled the challenges of microgrids under secondary cooperative control, focusing on operation constraints and clock drifts. Our comprehensive approach includes a detailed cyber-physical microgrid model and conditions ensuring reliable performance in transient and steady states amidst clock drifts and load changes. We introduced a novel algorithm for fine-tuning parameters within the secondary control scheme, effectively minimizing steady-state errors caused by clock drift while maintaining transient operation quality. Rigorous experiments validated the effectiveness of our methods.

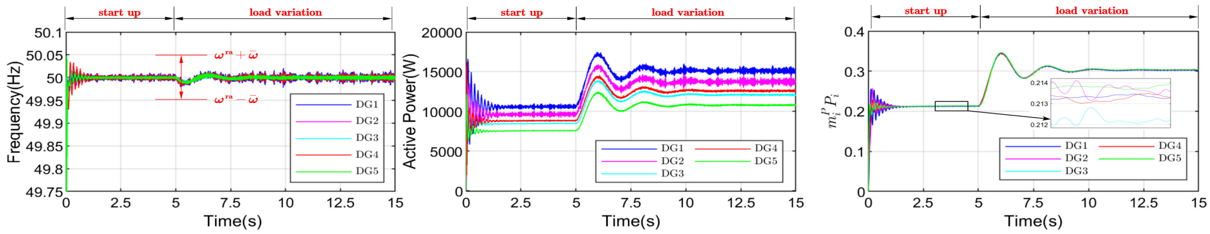

Fig. 3. Frequency and active response under all conditions in (39) met.

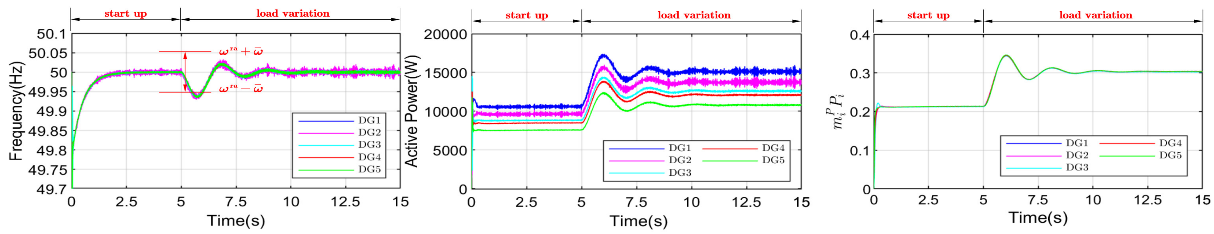

Fig. 4. Frequency and active power response under the condition where the third condition in (39) is not satisfied.

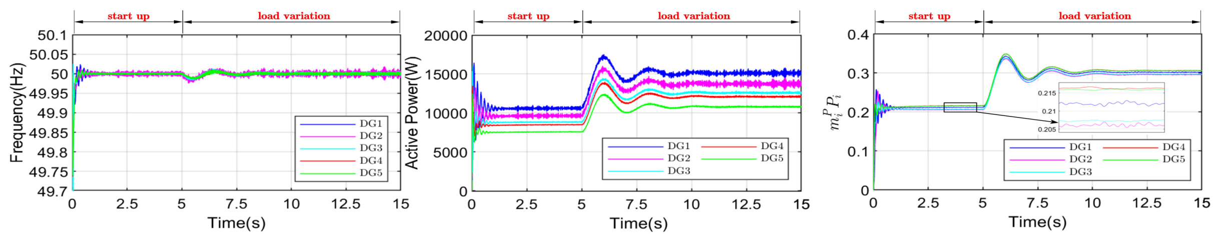

Fig. 5. Frequency and active power response under the condition where the second condition in (39) is not satisfied.

REFERENCES

[1] Song Q, Liu X, Sun L, Yang X, Xie S. Short-term load forecasting for electric power systems using the PSO-SVM and FCM clustering techniques. Electric Power Systems Research 2015;119:138-148.

[2] Tian H, Li X, Song J, Chen M, Zou L. Short-Term Wind Speed Forecasting Based on PSO and SVM. Energy Procedia 2017;105:1475-1480.

[3] Gao K, Wang T, Han C, et al. A review of optimization of microgrid operation. Energies 2021;14(10):2842.

[4] Brogan PV, Best RJ, Morrow DJ, McKinley K, Kubik ML. Effect of BESS Response on Frequency and RoCoF During Underfrequency Transients. IEEE Transactions on Power Systems 2019;34(1):575-583.

[5] K. S. Ratnam, K. Palanisamy, G. Yang. Future low-inertia power systems: Requirements, issues, and solutions-A review. Renewable and Sustainable Energy Reviews, 2020, 124: 109773.

[6] Y. Du, X. Lu, J. Wang and S. Lukic, Distributed Secondary Control Strategy for Microgrid Operation with Dynamic Boundaries, IEEE Transactions on Smart Grid, vol. 10, no. 5, pp. 5269-5282, Sept. 2019.

[7] Cordova S, Canizares CA, Lorca A, Olivares DE. Frequency-Constrained Energy Management System for Isolated Microgrids. IEEE Transactions on on Smart Grid 2022;13(5):3394-3407.

[8] Z. Chu, N. Zhang and F. Teng, Frequency-Constrained Resilient Scheduling of Microgrid: A Distributionally Robust Approach, IEEE Transactions on Smart Grid, vol. 12, no. 6, pp. 4914-4925, Nov. 2021.

[9] Han H, Chen X, Liu Z, Liu Y, Su M, Chen S. A Completely Distributed Economic Dispatching Strategy Considering Capacity Constraints. IEEE Journal on Emerging and Selected Topics in Circuits and Systems 2021;11(1):210-221.

[10] P. Martí, J. Torres-Martínez, C. X. Rosero, M. Velasco, J. Miret and M. Castilla, Analysis of the Effect of Clock Drifts on Frequency Regulation and Power Sharing in Inverter-Based Islanded Microgrids, IEEE Transactions on Power Electronics, vol. 33, no. 12, pp. 10363-10379, Dec. 2018.

[11] J. Schiffer, R. Ortega, C. A. Hans and J. Raisch, Droop-controlled inverter-based microgrids are robust to clock drifts, 2015 American Control Conference (ACC), Chicago, IL, USA, 2015, pp. 2341-2346.

[12] M. Castilla, A. Camacho, P. Martí, M. Velasco and M. M. Ghahderijani, Impact of Clock Drifts on Communication-Free Secondary Control Schemes for Inverter-Based Islanded Microgrids,IEEE Transactions on Industrial Electronics, vol. 65, no. 6, pp. 4739-4749, June 2018.

[13] J. Torres-Martínez, M. Castilla, J. Miret, M. Moradi-Ghahderijani and J. M. Rey, Experimental study of clock drift impact over droop-free distributed control for industrial microgrids, IECON 2017 - 43rd Annual Conference of the IEEE Industrial Electronics Society, Beijing, China, 2017, pp. 2479-2484.

[14] Kolluri, R. R., Mareels, I., Alpcan, T., Brazil, M., de Hoog, J., and Thomas, D. A. (2018). Stability and active power sharing in droop controlled inverter interfaced microgrids: Effect of clock mismatches. Automatica, 93, 469-475.

[15] A. Krishna, J. Schiffer and J. Raisch, A Consensus-Based Control Law for Accurate Frequency Restoration and Power Sharing in Microgrids in the Presence of Clock Drifts, 2018 European Control Conference (ECC), Limassol, Cyprus, 2018, pp. 2575-2580.

[16] Contzen, M. P. (2020). Consensus based synchronization of clocks to diminish the effect of clock drifts in microgrids. IFAC-PapersOnLine, 53(2), 12980-12985.

[17] Hale J K. Ordinary differential equations. Courier Corporation, 2009.